Advancement of simplified modelling strategies for 3D phenomena and/or boundaries conditions for base-isolated buildings or specific soil-structure interactions.

Stéphane Grange, Panagiotis Kotronis, Jacky Mazars

Stéphane Grange, Panagiotis Kotronis, Jacky Mazars. Advancement of simplified modelling strategies for 3D phenomena and/or boundaries conditions for base-isolated buildings or specific soil-structure interactions.. [Research Report] Deliverable 67, 3S-R. 2006. hal-00102513

HAL Id: hal-00102513
https://hal.science/hal-00102513
Submitted on 3 Oct 2006

Priority 1.1.6.3

Global Change and Ecosystems

Project No.: GOCE-CT-2003-505488

LESSLOSS

Risk Mitigation for Earthquakes and Landslides
Integrated Project

Sixth Framework Programme

Priority 1.1.6.3 Global Change and Ecosystems

Deliverable Report

Deliverable [67] – Advancement of simplified modelling strategies for 3D phenomena and/or boundaries conditions for base-isolated buildings or specific soil-structure interactions

Sub-Project 8 – Displacement-based Design Methodologies

Deliverable/Task Leader: INPG Revision: Final

September, 2006

Project co-funded by the European Commission within the Sixth Framework Programme (2002-2006)		
Dissemination Level		
PU	Public	X
PP	Restricted to other programme participants (including the Commission Services)	
RE	Restricted to a group specified by the consortium (including the Commission Services)	
CO	Confidential, only for members of the consortium (including the Commission Services)	

PREFACE

Soil-Structure Interaction (SSI) is an important phenomenon that one has to take into account in building design. Structures resting on shallow strip foundations behave differently than structures constructed on piles. Several approaches exist to take this interaction into account: the "macro element" approach is one of particular interest. The macro element studied in this report is a 3D model of a circular and rigid foundation adequate for static, cyclic or dynamic loading. It takes into account the plasticity of the soil and the rocking of the foundation.

The model is very easy to use, requires low computational power and therefore it is well suited for structural design. It is implemented into FedeasLab, a finite element toolbox of Matlab developed at UC Berkeley [Filippou et al., 2004].

Comparisons with experimental results under, static [Gottardy et al., 1999], cyclic [TRISEE, 1998] and dynamic loading [CAMUS, 1997] show the good performance of the 3D macro element for simulating SSI phenomena.

At the last part of this report the 3D macro element is used to reproduce the behaviour of base isolators and dissipative devices. Comparison with experimental results shows once again the advantages of the approach.

ACKNOWLEDGEMENTS

The work presented in this deliverable has been undertaken in Institut National Polytechnique de Grenoble (INPG) by PhD student Stéphane Grange, Assist. Prof. Panagiotis Kotronis and Prof. Jacky Mazars.

TABLE OF CONTENTS

LIST OF TABLES

LIST OF FIGURES

LIST OF SYMBOLS AND ABBREVIATIONS

a,b,c,d,e,f = Parameters defining the shape and the size of the loading surface and the failure criterion

D = Diameter of the foundation

E^* = Space where reduced horizontal forces are divided by $aV'^c(\gamma - V')^d$ and moments by $bV'^e(\gamma - V')^f$

$d\vec{F}^*$ = Force increment in space E^*

f^∞ = Failure criterion

f_c = Loading surface

F = Current loading point

$F^{*\infty}$ = Final predicted loading point in space E^*

g = Flow rule

$\vec{h}(F,\vec{q})$ = Hardening function

H = Plastic modulus

$H_{x,y}$, $H'_{x,y}$ = Horizontal force, reduced horizontal force in directions x and y respectively

$H^*_{x,y}$, $M^*_{x,y}$ = Horizontal force, moment in space E^* in directions x and y respectively

K^{el} = Elastic tangent stiffness matrix

$M_{x,y}$, $M'_{x,y}$ = Moment, reduced moment in directions x and y respectively

q_{max} = Ultimate pressure of the foundation under vertical centre load

$\vec{q}$ = Hardening generalized array

u^{el}, u'^{el} = Elastic displacement array, reduced elastic displacement array

u^{pl}, u'^{pl} = Plastic displacement array, reduced plastic displacement array

$u'^{el}_{x,y}$ = Reduced horizontal elastic displacements

$u'^{pl}_{x,y}$ = Reduced horizontal plastic displacements

V, V' = Vertical force, reduced vertical force

$\alpha, \beta, \delta, \eta$ = Kinematic hardening variables for dof $(u_x', \theta_x', u_y', \theta_y')$ respectively

γ = 2nd root on axis V' of the current loading surface

$\vec{\tau}$ = Kinematic hardening array containing the current values of the hardening variables

$\|\vec{\tau}\|$ = Norm of the vector $\vec{\tau}$

$\vec{\tau}_{\mathrm{lim}}$ = Kinematic hardening array containing the limits of the hardening variables

$\theta'^{el}_{x,y}$ = Reduced horizontal elastic rotations

$\theta'^{pl}_{x,y}$ = Reduced horizontal plastic rotations

ρ = Isotropic hardening variable

1. INTRODUCTION

In structural engineering, Soil-Structure Interaction (SSI) is an important phenomenon that has to be taken into account. Before proceeding to the design of slender structures like buildings or bridge piers, it is necessary to define the characteristics of the soil, of the structure itself as well as the nature of the connection between them. It is evident that the behaviour of a structure is different if it is embedded in the soil or just connected with a knee joint.

Different experimental results [CAMUS, 1997] showed that non linearities at the soil level (plasticity) and between the soil and the foundation (rocking and uplift of the foundation) result often to an isolation of the structure and thus to a reduction of the forces and the moments developed at its base during an earthquake. Maximum values of stresses are limited because of larger energy dissipation but more important displacements are generated at the top.

In order to study the SSI, three kinds of methods can be found in the literature [Pecker, 1984]:

- "Sub structuring" that aims at decomposing the problem into simpler problems (Kausel's superposition principle: kinematics interaction, inertial interaction). This method is valid only for linear problems.
- "Direct methods" that use a classical finite element approach. They provide very good results but require numerical expertise, good knowledge of the constitutive laws and are costly in terms of computational power.
- "Hybrid methods" that are a combination of the two previous methods and therefore more attractive on the numerical level. The "macro element" approach belongs to this last category and consists in condensing all non linearities into a finite domain, thus allows working with global variables.

Several 2D macro elements exist in the literature [Nova et al. 1991], [Cassidy et al. 2002], [Crémer 2001], [Crémer et al. 2001], [Crémer et al. 2002]. They allow simulating in a very simple way the behaviour of shallow foundations using only forces and displacements. The macro element developed by Crémer is able to reproduce the behaviour of a slender structure under static/cyclic but also dynamic loading (i.e. earthquake) applied in the horizontal direction, considering the plasticity of the soil and the rocking and uplift of the foundation.

Inspired by her work, a new 3D macro element is developed and presented in this report. The goal is to compute the 3D behaviour of a shallow and rigid foundation, lying on an infinite space under an earthquake applied in the 2 horizontal directions. The macro element takes into account the plasticity of the soil (resulting from the thermodynamics of irreversible processes), and the rocking of the structure. It is implemented into FedeasLab, a finite element Matlab toolbox developed by Pr. F. Filippou and his co-workers in UC Berkeley [Filippou et al., 2004].

At the beginning of this report we discuss the geometrical characteristics of the studied foundation and its behaviour under a cyclic loading, if rocking and uplift of its centre are permitted. Then the mathematical description of the 3D macro element is presented followed by the presentation of numerical results compared with experimental data found in the literature.

At the last part of this report, an adaptation of the 3D macro element is presented in order to reproduce the non linear behaviour of different base isolators and dissipation devices. Again, comparison with experimental results shows the good performance of the approach.

2. SHAPE OF THE FOUNDATION AND ASSOCIATED KINEMATIC VARIABLES

In order to simplify the problem, the foundation studied hereafter is considered circular. The horizontal loads in the directions x and y are therefore computed in a similar way. It is also easier to reproduce the interaction between horizontal forces and moments. The foundation is also considered shallow and rigid (Figure 2.1). Torsional moment (M_z) is not taken into account by the model.

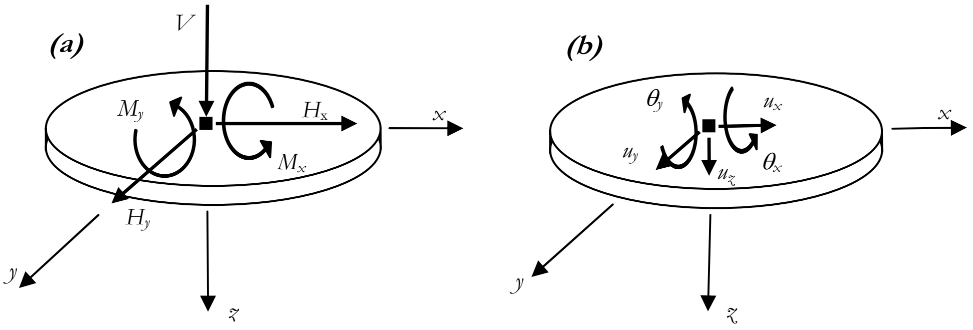

Figure 2.1. Shape of the foundation and generalized variables: (a) forces and (b) displacements.

The macro element concept consists in condensing the global behaviour of the foundation (or in general the structural element studied) in a representative point. One distinguishes the close field, located at the vicinity of the foundation, where all non-linearities and their couplings are concentrated [Crémer, 2001] and the far field, where all the sources of radiative damping are assumed. The far field is considered linear. In that framework it is appropriate to work with global variables (forces and displacements). The movement of the foundation, supposed hereafter infinitely rigid, is therefore entirely described by a system of global variables defined in the foundation centre: the vertical force V, horizontal forces H_x, H_y, and moments M_x M_y but also the corresponding displacements: vertical settlement u_z, horizontal displacements u_x, u_y, and rotations θ_x, θ_y.

In order to simplify the equations and to be able to compare the results, an adimensional notation of variables is used as follows:

- Reduced horizontal forces: H'_x, H'_y

- Reduced vertical force: V'
- Reduced moments: M'_x, M'_y

With
$$F=\begin{pmatrix} V' \\ H'_x \\ M'_y \\ H'_y \\ M'_x \end{pmatrix}=\frac{1}{\frac{\pi D^2}{4}q_{\max}}\begin{pmatrix} V \\ H_x \\ \frac{M_y}{D} \\ H_y \\ \frac{M_x}{D} \end{pmatrix} \tag{1.1}$$

In a similar way we get for the displacements:

- Reduced horizontal displacements: u'_x, u'_y
- Reduced vertical displacement: u'_z
- Reduced rotations: θ'_x, θ'_y

$$u=\begin{pmatrix} u'_z \\ u'_x \\ \theta'_y \\ u'_y \\ \theta'_x \end{pmatrix}=\frac{1}{D}\begin{pmatrix} u_z \\ u_x \\ D\theta_y \\ u_y \\ D\theta_x \end{pmatrix} \tag{1.2}$$

With: q_{max} being the ultimate stress of the soil and D the diameter of the foundation.

3. BEHAVIOUR OF THE FOUNDATION UNDER CYCLIC LOADING

This 3D macro element aims to reproduce the behaviour of a shallow circular infinite rigid foundation lying on an infinite space under cyclic and dynamic loadings. The fundamental characteristics of the cyclic behaviour of the foundation have been presented in detail in [Crémer, 2001]. Only the main features are recalled hereafter.

A non symmetrical plasticity is created due to the rocking (rotation) and uplift (vertical negative displacement of the centre) of the foundation (Figure 3.1). Indeed, when the foundation undergoes a loading in the right direction ($dM<0$), it is considered that only the soil under the right part of the foundation is plastified, no stresses are developed under the left part. When the sign of the loading is reversed ($dM>0$), only the soil under the left part of the foundation is assumed plastified. The soil under the right part remains in the same plastic state reached during the previous phase. If a third loading is applied ($dM<0$), the soil under the right part of the foundation is again plastified but starting from the plastic state obtained during the first phase ($dM<0$). This is clearly shown in the Figure 3.1

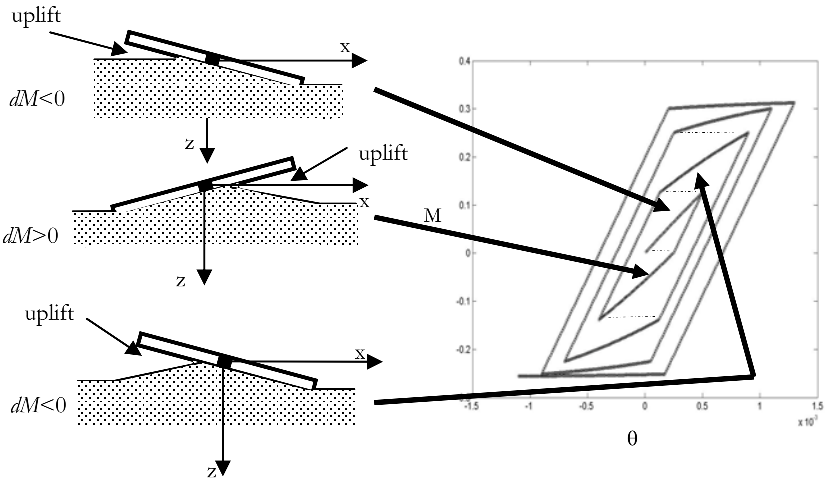

Figure 3.1. Behaviour of the foundation under a cyclic loading when rocking and uplift are permitted.

The choices for the failure criterion and for the nature and evolution of the loading surfaces are driven by this specific behaviour. It will be shown that the failure criterion chosen is appropriate for a mechanism of rocking with uplift. The hardening laws are isotropic and kinematic using independent variables for each direction of solicitation. The isotropic and kinematic hardenings are linked with a specific relation also provided in this report.

4. DESCRIPTION OF THE 3D MACRO ELEMENT

The 3D macro element developed hereafter is able to reproduce the behaviour of a shallow circular and rigid foundation under cyclic and dynamic loadings considering plasticity in the soil and rocking of the foundation.

The plasticity model is obtained within the framework of classical thermodynamics laws of irreversible processes. The load surface and the failure criterion come from the work of [Crémer, 2001] and are written in generalized variables V, H_x, M_x, H_y, M_y. Plasticity is coupled with uplift as the failure surface is defined for an overturning mechanism with uplift.

There are described hereafter:

- The elastic behaviour
- The plastic behaviour (the failure criterion, the loading surfaces, the kinematic and isotropic hardening rules, the tangency rule, the flow rule)

4.1 ELASTIC BEHAVIOUR

Thanks to the circular shape of the foundation, the stiffnesses corresponding to both horizontal displacements are the same. The same stands for the rotations. Using the adimensional notation presented previously, the following stiffness matrix is found (Equation (1.3)):

$$
\begin{aligned}
K^{el} &= \begin{pmatrix} K'^{el}_{zz} & 0 & 0 & 0 & 0 \\ 0 & K'^{el}_{hh} & 0 & 0 & 0 \\ 0 & 0 & K'^{el}_{\theta\theta} & 0 & 0 \\ 0 & 0 & 0 & K'^{el}_{hh} & 0 \\ 0 & 0 & 0 & 0 & K'^{el}_{\theta\theta} \end{pmatrix} \\
&= \begin{pmatrix} \frac{K^{el}_{zz}D}{Sq_{\max}} & 0 & 0 & 0 & 0 \\ 0 & \frac{K^{el}_{hh}D}{Sq_{\max}} & 0 & 0 & 0 \\ 0 & 0 & \frac{K^{el}_{\theta\theta}}{DSq_{\max}} & 0 & 0 \\ 0 & 0 & 0 & \frac{K^{el}_{hh}D}{Sq_{\max}} & 0 \\ 0 & 0 & 0 & 0 & \frac{K^{el}_{\theta\theta}}{DSq_{\max}} \end{pmatrix}
\end{aligned}
\qquad (1.3)
$$

As was the case for the 2D macro element [Crémer, 2001], this stiffness matrix is calculated using the real part of the static impedances of the foundation [Gazetas, 1991].

4.2 PLASTIC BEHAVIOUR

4.2.1 Failure criterion

The failure criterion is defined for an overturning mechanism with uplift. It comes from the works of [Pecker, 1997] and it has been used already in the 2D macro element [Crémer, 2001]. This criterion was initially developed for a shallow strip and rigid foundation in 2D lying on a half space of homogeneous cohesion. However, [Gottardy et al., 1999] showed that the shapes of the load and failure surfaces for a circular footing are very similar.

The adaptation of the previous criterion in 3D is feasible because the foundation studied presents symmetry of revolution. Therefore, the horizontal forces H'_x and H'_y on the one hand and the moments M'_x, M'_y on the other hand are treated in a similar manner, i.e. the interactions between the two horizontal forces or the two moments are described by circles. At the end, a 5D surface is obtained by adding to the original criterion two terms, the first dealing with the horizontal force H'_y and the second with the moment M'_x (Equation (1.4)).

The equation of the failure criterion is the following:

$$
\begin{aligned}
f_\infty \equiv & \left(\frac{H'_x}{aV'^c (1-V')^d} \right)^2 + \left(\frac{M'_y}{aV'^e (1-V')^f} \right)^2 \\
& + \left(\frac{H'_y}{aV'^c (1-V')^d} \right)^2 + \left(\frac{M'_x}{bV'^e (1-V')^f} \right)^2 - 1 = 0
\end{aligned}
\tag{1.4}
$$

With the coefficients:

- *a*, *b* defining the size of the surface in the planes $(H' - M')$
- c, d, e and f defining the parabolic shape of the surface in the planes $(V' - M')$ and $(V' - H')$

Theses parameters can be fitted in order to reproduce different experimental results found in the literature (see for example the numerical simulations in paragraph 5).

4.2.2 Loading surfaces

The loading surfaces must be able to treat independently the vertical force on the one hand and the horizontal forces and moments on the other hand. This is clearly understood looking at the failure criterion (Equation (1.4)): the interaction between H' and M' is a perfect ellipse centred on the origin of the space, whereas the interaction between H' and V' is a curve passing by the origin of the space and defined only for $V' > 0$.

A variable γ is chosen to parameterize the second intersection point of the curve with the V' axis (the other point is the origin of the space) and the evolution of the loading surface according to this axis. This hardening variable gives the maximum vertical load that the structure supported throughout the whole history of the loading (most of the time it is equal to the weight of the structure).

In order to parameterize the size of the ellipse in the hyper plane (H'_x, M'_y, H'_y, M'_x), two kinds of hardening laws - one kinematic (τ) and one isotropic (ρ) - are used. This description is essential in order to reproduce the cyclic behaviour seen before.

The analytical expression of the loading surface - represented in Figure 4.1 as a 3D projection in a space (V', M', V') - takes finally the following form:

$$
\begin{aligned}
f_c(F,\vec{\tau},\rho) \equiv & \left(\frac{H'_x}{\rho a V'^{c} (\gamma - V')^{d}} - \frac{\alpha}{\rho} \right)^2 + \left(\frac{M'_y}{\rho a V'^{e} (\gamma - V')^{f}} - \frac{\beta}{\rho} \right)^2 \\
& + \left(\frac{H'_y}{\rho a V'^{c} (\gamma - V')^{d}} - \frac{\delta}{\rho} \right)^2 + \left(\frac{M'_x}{\rho b V'^{e} (\gamma - V')^{f}} - \frac{\eta}{\rho} \right)^2 - 1 = 0
\end{aligned}
\tag{1.5}
$$

Where $\alpha, \beta, \delta, \eta$ are the kinematic hardening variables and ρ the isotropic hardening variable. The relationships driving the evolution of theses hardening variables are given in the following paragraphs.

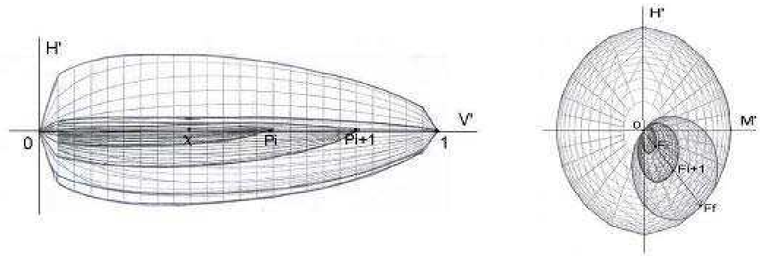

Figure 4.1. Failure criterion and evolution of the loading surfaces projected in a 3D space (H', M', V') [Crémer, 2001].

4.2.3 Kinematic hardening rule

Kinematic variables $\alpha, \beta, \delta, \eta$ permit to determine the centre of the ellipse in the hyper plane. The evolution of theses variables has been obtained by studying the experimental and numerical behaviour of a foundation under a monotonic static loading. More specifically, [Gottardy et al., 1999] provide the relations for a circular footing and for different kinds of soils (obtained from experimental tests) and [Crémer, 2001] uses similar curves (obtained with FEM simulations) to fit her model. Figure 4.2 shows for example the relation between the moment M' and the rotation θ'.

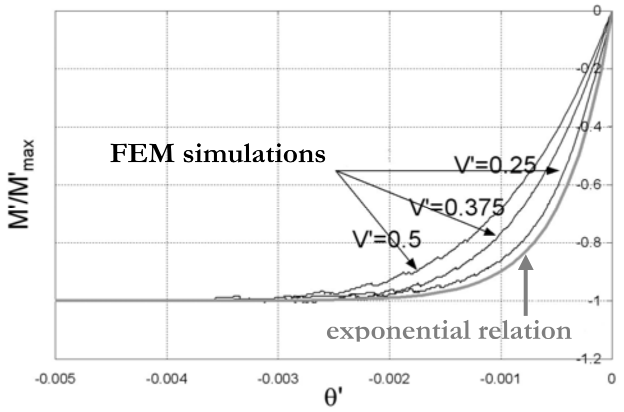

Figure 4.2. Relationship between moment and rocking angle using numerical simulations with the code Dynaflow [Crémer, 2001].

It comes out that the different relationships between forces/moments and associated displacements/rotations can be approached using exponential relations, driven by a 1st order differential equation. For example, the relationship between M'_y and θ'_y can be approached as follows:

$$\frac{dM'_y}{d\theta'_y} = K'^{el}_{\theta\theta}\exp\left(\frac{-K'^{el}_{\theta\theta}}{M'^{\infty}_y}\theta'_y\right) \tag{1.6}$$

Where M'^{∞}_y is the limit of the curve $M'_y\left(\theta'_y\right)$ when θ'_y tends to infinity. If (.) is the sign of the derivative with respect to time then Equation (1.6) is the solution of the following 1st order differential equation:

$$\Leftrightarrow \dot{M}'_y = K'^{el}_{\theta\theta}\left(1-\frac{M'_y}{M'^{\infty}_y}\right)\dot{\theta}'_y \tag{1.7}$$

Assuming the classical partition of the total displacement u into an elastic part u^{el} and a plastic part u^{pl} ($u = u^{el} + u^{pl}$), and considering that $\dot{M}'_y = K'^{el}_{\theta\theta}\,\dot{\theta}'^{el}_y$, it is easy to link the increment of force with the increment of the associated plastic displacement (Equation (1.8)):

$$\dot{M}'_y = K'^{el}_{\theta\theta}\left(\frac{M'^{\infty}_y}{M'_y} - 1\right)\dot{\theta}'^{pl}_y \tag{1.8}$$

Moreover, as M'_y can be represented in the same space as $\beta b V'^e(\gamma - V')^f$ (in Equation (1.5) - the two terms have the same size), the evolution of the kinematic hardening variable β is driven by the following relation:

$$\dot{\beta} = \frac{1}{bV'^e(\gamma - V')^f} K'^{el}_{\theta\theta}\left(\frac{M^{*\infty}_y}{\beta} - 1\right)\dot{\theta}'^{pl}_y \tag{1.9}$$

Where $M^{*\infty}_y$ is the limit of the curve $\beta\left(\dot{\theta}'^{pl}_y\right)$ when $\dot{\theta}'^{pl}_y$ tends to infinity. It is clear at this point that the evolutions of the other kinematic hardening variables are driven by similar relations.

As the behaviour is different for *dF*>0 and for *dF*<0, two families of kinematic hardening laws and variables are used to describe the evolution of each force. 8 relations and variables are therefore used in the model for the 8 forces dH'_x>0, dH'_x<0, dH'_y>0, dH'_y<0, dM'_x>0, dM'_x<0, dM'_y>0, dM'_y<0. For example for a radial loading, each kinematic hardening variable has the following expression (the case of β is only presented for simplicity):

$$\begin{cases} \dot{\beta}^{\oplus} = \dfrac{1}{bV'^e(\gamma - V')^f} K'^{el}_{\theta\theta}\left(\dfrac{M^{*\infty}_y}{\beta^{\oplus}} - 1\right)\dot{\theta}'^{pl}_y \\ \dot{\beta}^{\Theta} = \dfrac{1}{bV'^e(\gamma - V')^f} K'^{el}_{\theta\theta}\left(-\dfrac{M^{*\infty}_y}{\beta^{\Theta}} - 1\right)\dot{\theta}'^{pl}_y \end{cases} \tag{1.10}$$

The first equation of system (Equation (1.10)) is activated when $\dot{\theta}'^{pl}_y \geq 0$ (corresponding to the sign $\oplus$), the second equation when $\dot{\theta}'^{pl}_y < 0$ (corresponding to the sign Θ). Finally, at each step β is calculated following $\beta = \beta^{\oplus} + \beta^{\Theta}$.

For a non radial loading (i.e. when relations between forces and moments are not linear), the evolution is more complicated. Indeed, in many cases β_{lim} can decrease whereas $dM'_y \geq 0$ (β_{lim} being the limit value of β). In other words even if M'_y increases and $\dot{\theta}'^{pl}_y \geq 0$, β^{Θ} needs to be activated. This is the reason why for a non radial loading, the evolution of the kinematic hardening variables is driven by relations of the form:

$$\begin{cases} \dot{\beta}^{\oplus} = \dfrac{1}{bV'^{e}\left(\gamma - V'\right)^{f}} K'^{el}_{\theta\theta} \left(\dfrac{M_y^{*\infty}}{\beta^{\oplus}} - 1 \right) \left| \dot{\theta}'^{pl}_{y} \right| \\ \dot{\beta}^{\Theta} = -\dfrac{1}{bV'^{e}\left(\gamma - V'\right)^{f}} K'^{el}_{\theta\theta} \left(-\dfrac{M_y^{*\infty}}{\beta^{\Theta}} - 1 \right) \left| \dot{\theta}'^{pl}_{y} \right| \end{cases} \tag{1.11}$$

The first equation of the system (Equation (1.11)) is activated when $d\beta \geq 0$ while the second equation when $d\beta \leq 0$. The sign of $d\beta$ is identical to the sign of $\beta_{\lim} - \beta$. The tangency rule explained in the next paragraph provides us with β_{lim}, as for β it is the one calculated during the previous step.

In order to use Equation (1.11), the value of $M_y^{*\infty}$ is also needed. It is evaluated as follows:

$$\begin{cases} M_y^{*\infty} = \beta_{\lim} - \beta^{\Theta} & \mathit{if} \quad d\beta > 0 \\ M_y^{*\infty} = -\left(\beta_{\lim} - \beta^{\oplus}\right) & \mathit{if} \quad d\beta < 0 \end{cases} \tag{1.12}$$

Note: the limit $M_y^{*\infty}$ is always positive, less or equal to 1.

4.2.4 Tangency rule

In case of a non radial loading, the final loading point isn't known as it can be anywhere on the failure criterion. Moreover, the evolution of the loading surfaces has to be specified, as there is a risk of interpenetration with the failure criterion (even if the loading point has not yet reached it).

Consequently, the tangency rule has two functions: first, it permits to determine the final loading point and the limits of the kinematic hardening variables and second, it ensures that the loading surface is tangent to the failure criterion at the final loading point. In other words, the loading surface never interpenetrates the failure criterion: failure occurs the first time the loading point intercepts it.

This rule is described in the space $E^{*}=(H^{*}_{x}, M^{*}_{y}, H^{*}_{y}, M^{*}_{y})$ where:

$$\begin{cases} H_x^* = \dfrac{H'_x}{aV'^c\left(\gamma - V'\right)^d} \\ M_y^* = \dfrac{M'_y}{bV'^e\left(\gamma - V'\right)^f} \\ H_y^* = \dfrac{H'_y}{aV'^c\left(\gamma - V'\right)^d} \\ M_x^* = \dfrac{M'_x}{bV'^e\left(\gamma - V'\right)^f} \end{cases} \tag{1.13}$$

From Equation (1.13) it is obvious that in this space the loading surfaces are circles with centre at the extremity of the vector $\vec{\tau} = {}^t\left[\alpha \quad \beta \quad \delta \quad \eta\right]$ and radius ρ. They evolve inside the failure criterion which is also a circle when γ=1 (Figure 4.3).

The tangency rule adopted is based on the assumption that the final loading point ($F^{*\infty}$) is given by the projection of the current loading point (F^*) on the failure criterion in the direction of the current increment of force (dF^*). Thus the centre of the final circle is the extremity of the vector $\vec{\tau}_{\lim} = {}^t\left[\alpha_{\lim} \quad \beta_{\lim} \quad \delta_{\lim} \quad \eta_{\lim}\right]$ and it is a point on the radius of the failure criterion (when $\gamma = 1$). $\vec{\tau}_{\lim}$ is predicted considering the evolution of the size of the loading surface of the next step. The radius of the circle increases in a similar manner with the movement of the centre of the loading surface. Several iterations are necessary to predict $\vec{\tau}_{\lim}$.

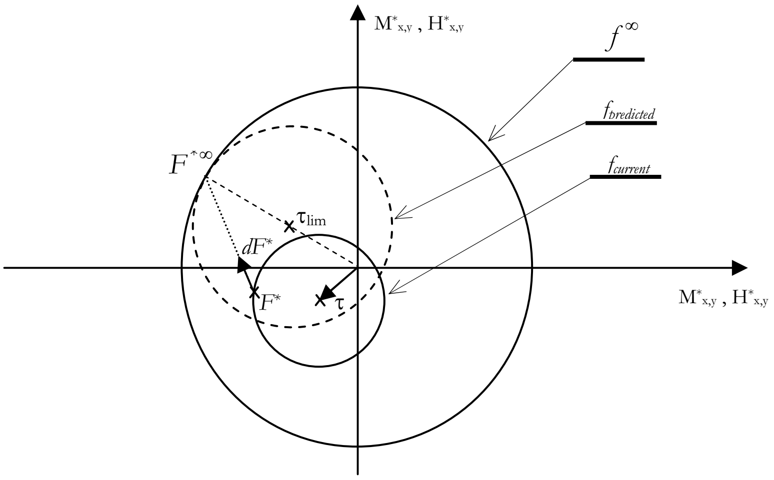

Figure 4.3. Non interpenetration criterion (projection in a 2D plane *(H*, M*)*) – determination of the final loading point.

4.2.5 Isotropic hardening rule

The independence of the directions (for *dM*>0 and *dM*<0) is taken into account using the specific kinematic hardening laws described in the previous paragraphs. However, another property of the behaviour of the foundation under cyclic loading permits to link the isotropic with the kinematical hardening laws [Crémer, 2001]. Indeed, when a plastic state is reached during a new cycle, plastic behaviour is recovered at the same state (and with the same slope) as before. The evolution of the loading surfaces describing this property is given in Figure 4.4.

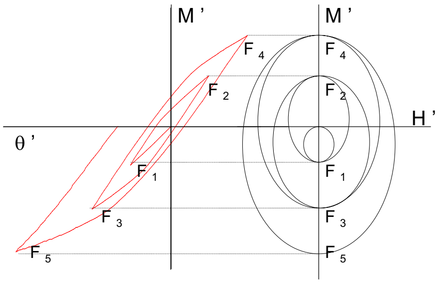

Figure 4.4. Evolution of the loading surfaces considering a radial loading [Crémer, 2001].

This property is translated into the mathematical relation:

$$\dot{\rho} = \left\| \dot{\vec{\tau}} \right\| \tag{1.14}$$

With:

$$\left\| \dot{\vec{\tau}} \right\| = \left| \frac{\alpha\dot{\alpha} + \beta\dot{\beta} + \delta\dot{\delta} + \eta\dot{\eta}}{\sqrt{\alpha^2 + \beta^2 + \delta^2 + \eta^2}} \right| \tag{1.15}$$

Note: the influence of rocking/uplift can be reduced or cancelled by choosing an arbitrary evolution of the isotropic hardening variable as follows:

$$\dot{\rho} = k \times \left\| \dot{\vec{\tau}} \right\| \tag{1.16}$$

Where $0 \le k \le 1$

4.2.6 Evolution of γ

The parameter γ characterizes the second root of the loading surface on the V' axis and represents the maximum vertical load the structure has supported during the whole loading history. It is equal, most of the time, to the weight of the structure. Its evolution is therefore closely dependant on the evolution of the vertical force V', at least for the initialisation phase, where the foundation is submitted only to the weight of the structure. During this phase $\gamma = V'$.

The evolution of γ is driven by the empirical relationship linking vertical force and vertical displacement given by [Nova and Montrasio, 1991]:

Thus for a monotonic loading: $\gamma = 1 - \exp\left(-K'^{el}_{zz}\left(1 - u'_z\right)\right)$

Which can be written as a 1st order differential equation:

$$\dot{\gamma} = K'^{el}_{zz}\left(1-\gamma\right) \tag{1.17}$$

Nevertheless, the other plastic displacements (horizontal displacements and rotations) can also increase the size of the loading surfaces in the direction of V'. Consequently, the evolution of γ depends also on them and γ is driven by the following expression.

$$\dot{\gamma} = K'^{el}_{zz}\left(a_1\dot{u}'^{pl}_z + a_2\dot{u}'^{pl}_x \; a_3\dot{\theta}'^{pl}_z \; a_4\dot{u}'^{pl}_y \; a_5\dot{\theta}'^{pl}_z\right)\left(1-\gamma\right) \tag{1.18}$$

Where a_1, a_2, a_3, a_4 and a_5 are parameters which permit to adjust the influence of each component of the plastic displacement array.

4.2.7 Flow rule

In the 4D space defining by the hyper plane (H'_x, M'_y, H'_y, M'_x), plasticity develops according to the normal at the loading surface, i.e. if the projection of the normal on a given axis (H'_x) is positive, the associated plasticity (u'^{pl}_x) is also positive (Figure 4.5). The loading surface f_c is thus sufficient to describe the direction of the plasticity velocity and the flow rule in this hyper plane is associated.

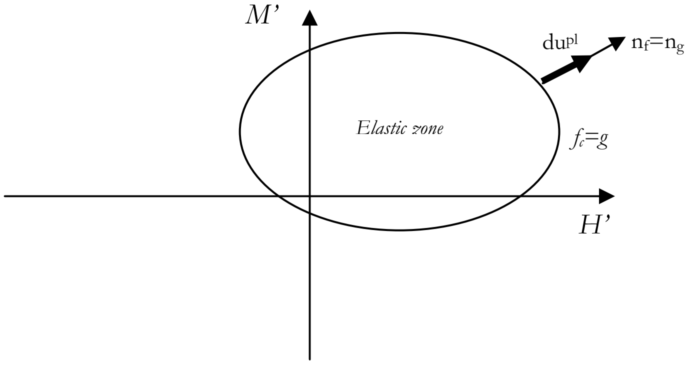

Figure 4.5. Representation of the flow rule in (M' – H') plane

In the other 4 planes where the vertical force V' interferes *(i.e.* (H'_x, V'), (M'_y, V'), (H'_y, V'), (M'_x, V')), the loading surface cannot be used to determine the direction of the plasticity velocity. Indeed, there are cases where the normal at this surface is of a negative value whereas the plasticity velocity $\dot{u}_z^{pl}$ is always positive or equal to zero (Figure 4.6).

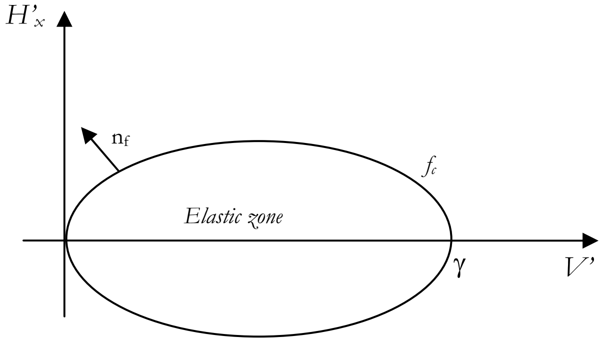

Figure 4.6. Representation of the loading surface in (H' – V') plane – projection of n_f on V' axis can be negative

This is the reason why a non-associated flow rule is used in theses 4 planes. The expression of g is the following:

$$g\left(F,\vec{\tau},\rho,V'_0\right)\equiv\left(\frac{H'_x}{\rho\frac{aV'^c}{\left(\kappa\gamma+V'_0\right)}\left(\gamma-V'\right)^d\left(\kappa\gamma+V'\right)^d}-\frac{\alpha}{\rho}\right)^2$$
$$+\left(\frac{M'_y}{\rho\frac{bV'^e}{\left(\xi\gamma+V'_0\right)}\left(\gamma-V'\right)^f\left(\xi\gamma+V'\right)^f}-\frac{\beta}{\rho}\right)^2$$
$$+\left(\frac{H'_y}{\rho\frac{aV'^c}{\left(\kappa\gamma+V'_0\right)}\left(\gamma-V'\right)^d\left(\kappa\gamma+V'\right)^d}-\frac{\delta}{\rho}\right)^2$$
$$+\left(\frac{M'_x}{\rho\frac{bV'^e}{\left(\xi\gamma+V'_0\right)}\left(\gamma-V'\right)^f\left(\xi\gamma+V'\right)^f}-\frac{\eta}{\rho}\right)^2-1=0 \tag{1.19}$$

Where V'_0 is the current vertical force used in order to assure that the flow rule *g* and the loading surface f_c have their intersection on the loading point *F*.

f_c et *g* are therefore identical in the planes (H'_x, M'_y), (H'_x, M'_x), (H'_x, H'_y), (M'_y, M'_x), $(M'_y,\ H'_y)$, $(M'_x,\ H'_y)$ (i.e. ellipse), whereas f_c and *g* are non associated in (H'_x, V'), (M'_y, V'), (H'_y, V'), (M'_x, V').

The representation of *g* in the plane $(M'_y\text{-}V')$ is given in the Figure 4.7.

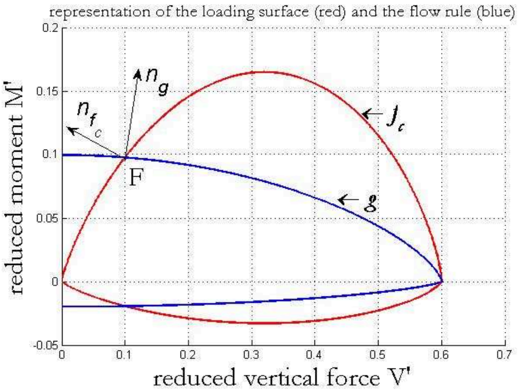

Figure 4.7. Representation of the computed flow rule and the loading surface for a given loading point F in the planes (M' - V') and (H' - V').

The horizontal tangent of the flow rule can be adjusted using 2 parameters ξ and χ in order to modify the evolutions of plastic displacements in the hyper plane $(u'_x, \theta'_y, u'_y, \theta'_x)$ compared to the vertical plastic displacement. In the general case, the horizontal tangent in $(M'\text{-}V')$ planes is located on $V' = \gamma(1-\xi)/2$ and the horizontal tangent in $(H'\text{-}V')$ planes is located on $V' = \gamma(1-\chi)/2$. In Figure 4.7 theses parameters are taken as default equal to 1 to obtain always an horizontal tangency for V' =0.

4.3 IMPLEMENTATION OF THE PLASTICITY MODEL

In this part, some details about the specific implementation of the plasticity model are given. Particularly tools and formulations needed to program the Return Mapping algorithm are recalled [Simo et al., 1998].

4.3.1 Normality rule

Following the classical plasticity theory, the direction of the plasticity velocity is given by the normality rule defined hereafter:

$$\dot{\vec{u}}^{pl} = \dot{\lambda}\frac{\partial g}{\partial F} \Leftrightarrow \begin{cases} \dot{u}_z^{pl} = \dot{\lambda}\dfrac{\partial g}{\partial V'} \\ \dot{u}_x^{pl} = \dot{\lambda}\dfrac{\partial g}{\partial H'_x} \\ \dot{\theta}_y^{pl} = \dot{\lambda}\dfrac{\partial g}{\partial M'_y} \\ \dot{u}_y^{pl} = \dot{\lambda}\dfrac{\partial g}{\partial H'_y} \\ \dot{\theta}_x^{pl} = \dot{\lambda}\dfrac{\partial g}{\partial M'_x} \end{cases} \tag{1.20}$$

Where $\dot{\lambda} \geq 0$

The hardening function $\vec{h}$ is defined as: $\dot{\vec{q}} = -\dot{\lambda}\vec{h}(F,\vec{q})$. This function is essential to the Return Mapping algorithm.

$$\dot{\vec{q}}=\begin{bmatrix}\dot{\alpha}^{\oplus}\\ \dot{\alpha}^{\Theta}\\ \dot{\beta}^{\oplus}\\ \dot{\beta}^{\Theta}\\ \dot{\delta}^{\oplus}\\ \dot{\delta}^{\Theta}\\ \dot{\eta}^{\oplus}\\ \dot{\eta}^{\Theta}\\ \dot{\rho}\\ \dot{\gamma}\end{bmatrix}=-\dot{\lambda}\begin{bmatrix}
v_{\alpha}^{\oplus}\dfrac{1}{aV'^{c}\left(\gamma-V'\right)^{d}}K'^{el}_{hh}\left(1-\dfrac{H'^{\infty}_{x}}{\alpha^{\oplus}}\right)\left|\dfrac{\partial g}{\partial H'_{x}}\right|\\
-v_{\alpha}^{\Theta}\dfrac{1}{aV'^{c}\left(\gamma-V'\right)^{d}}K'^{el}_{hh}\left(1+\dfrac{H'^{\infty}_{x}}{\alpha^{\Theta}}\right)\left|\dfrac{\partial g}{\partial H'_{x}}\right|\\
v_{\beta}^{\oplus}\dfrac{1}{bV'^{e}\left(\gamma-V'\right)^{f}}K'^{el}_{\theta\theta}\left(1-\dfrac{M'^{\infty}_{y}}{\beta^{\oplus}}\right)\left|\dfrac{\partial g}{\partial M'_{y}}\right|\\
-v_{\beta}^{\Theta}\dfrac{1}{bV'^{e}\left(\gamma-V'\right)^{f}}K'^{el}_{\theta\theta}\left(1+\dfrac{M'^{\infty}_{y}}{\beta^{\Theta}}\right)\left|\dfrac{\partial g}{\partial M'_{y}}\right|\\
v_{\delta}^{\oplus}\dfrac{1}{aV'^{c}\left(\gamma-V'\right)^{d}}K'^{el}_{hh}\left(1-\dfrac{H'^{\infty}_{y}}{\delta^{\oplus}}\right)\left|\dfrac{\partial g}{\partial H'_{y}}\right|\\
-v_{\delta}^{\Theta}\dfrac{1}{aV'^{c}\left(\gamma-V'\right)^{d}}K'^{el}_{hh}\left(1+\dfrac{H'^{\infty}_{y}}{\delta^{\Theta}}\right)\left|\dfrac{\partial g}{\partial H'_{y}}\right|\\
v_{\eta}^{\oplus}\dfrac{1}{bV'^{e}\left(\gamma-V'\right)^{f}}K'^{el}_{\theta\theta}\left(1-\dfrac{M'^{\infty}_{x}}{\eta^{\oplus}}\right)\left|\dfrac{\partial g}{\partial M'_{x}}\right|\\
-v_{\eta}^{\Theta}\dfrac{1}{bV'^{e}\left(\gamma-V'\right)^{f}}K'^{el}_{\theta\theta}\left(1+\dfrac{M'^{\infty}_{x}}{\eta^{\Theta}}\right)\left|\dfrac{\partial g}{\partial M'_{x}}\right|\\
-\left|\dfrac{\alpha\dfrac{1}{aV'^{c}\left(\gamma-V'\right)^{d}}K'^{el}_{hh}\left(v_{\alpha}^{\oplus}\left(\dfrac{H'^{\infty}_{x}}{\alpha^{\oplus}}-1\right)+v_{\alpha}^{\Theta}\left(\dfrac{H'^{\infty}_{x}}{\alpha^{\oplus}}+1\right)\right)\left|\dfrac{\partial g}{\partial H'_{x}}\right|+\ldots}{\sqrt{\alpha^{2}+\beta^{2}+\delta^{2}+\eta^{2}}}\right|\\
K'^{el}_{zz}\left(a_{1}\dfrac{\partial g}{\partial H'_{z}}+a_{2}\left|\dfrac{\partial g}{\partial H'_{x}}\right|a_{3}\left|\dfrac{\partial g}{\partial M'_{y}}\right|a_{4}\left|\dfrac{\partial g}{\partial H'_{y}}\right|a_{5}\left|\dfrac{\partial g}{\partial M'_{x}}\right|\right)\left(\gamma-1\right)
\end{bmatrix} \tag{1.21}$$

Variables $v_{\alpha}^{\oplus}$ and v_{α}^{Θ} permit to impose the zero value at variables $\dot{\alpha}^{\oplus}$ or $\dot{\alpha}^{\Theta}$, according to the current mode ($d\alpha>0$ or $d\alpha<0$).

Hardening variables are now linked with the normal at the flow rule and the plasticity multiplier λ. This multiplier is calculated thanks to the consistency rule described hereafter.

4.3.2 Consistency rule

The consistency rule translates the fact that the load point (the extremity of the vector force) is always on the load surface. It permits also to determine the plasticity multiplier λ as follows:

At each step and iteration both conditions $f = 0$ and $\dot{f} = 0$ have to be respected. The first condition can be written as:

$$
\begin{aligned}
\dot{f} = 0 \quad & \Leftrightarrow \quad \frac{\partial f}{\partial F} \cdot \dot{F} + \frac{\partial f}{q} \cdot \dot{q} = 0 \\
& \Leftrightarrow \quad \frac{\partial f}{\partial F} \cdot \dot{F} - \dot{\lambda} \frac{\partial f}{q} \cdot h = 0 \\
& \Leftrightarrow \quad \dot{\lambda} = \frac{\frac{\partial f}{\partial F} \cdot \dot{F}}{\frac{\partial f}{\partial q} \cdot h}
\end{aligned}
\qquad (1.22)
$$

This relation permits to introduce $H = \frac{\partial f}{\partial q} \cdot h$ as the plastic modulus.

The Return Mapping algorithm is finally used as follows:

4.3.3 Return Mapping Algorithm [Simo et al., 1998].

After determining a force using an elastic prediction (for step n and iteration i $F^{ni} = K^{el}\left(\vec{u}^{ni} - \vec{u}^{pl,ni}\right)$) the load point is out of the load surface. The Return Mapping Algorithm permits to bring back the force to the surface by increasing the hardening variables (implying an increase of the size of the surface and a displacement of its centre) and by reducing the elastic prediction till the solution points on the surface (the index of the return mapping is k).

$$F_k^{ni} = F_{k-1}^{ni} - K^{el}\delta(\Delta\lambda)\frac{\partial g}{\partial F} \tag{1.23}$$

$$q_k^{ni} = q_{k-1}^{ni} - \delta(\Delta\lambda)h \tag{1.24}$$

Where:

$$\delta(\Delta\lambda) = \frac{f_k^{ni}}{\frac{\partial f}{\partial F}\cdot K^{el}\cdot\frac{\partial g}{\partial F} + H} \tag{1.25}$$

The macro element is implemented in the Matlab toolbox FedeasLab [Filippou et al., 2004]. Numerical simulations are presented hereafter to evaluate the efficiency of this new tool.

5. NUMERICAL SIMULATIONS

The simulations are divided into 3 parts:

- To see whether the macro element is able to give good results under a static loading, numerical simulations are compared to experimental results coming from the works of [Gottardy et al., 1999].
- The performance of the macro element under a cyclic loading is then tested using the experimental results coming from the European program [TRISEE, 1998].
- Finally, in order to evaluate the efficiency of the macro element to predict the dynamic behaviour of a slender structure, the simulation of the Camus 4 experiment [Combescure et al., 2000] is carried out.

5.1 MONOTONIC STATIC BEHAVIOUR

Detailed presentation of the tests is presented in [Gottardy et al., 1999]. They concern a circular footing of diameter $2R=D=0.1$m lying on a sand of a known density.

At the beginning, a vertical displacement is applied at the foundation until a given vertical force is reached. Then, this vertical displacement is kept constant while another displacement (horizontal displacements or rotations or a combined displacement) is increasing. The test is thus completely displacement controlled. The response of the foundation is represented in the space of forces. The curve described in the space (H'_x, M'_y, H'_y, M'_x) is an approximation of the yield surface (Figure 5.1 - that's why the test is called "swipe test").

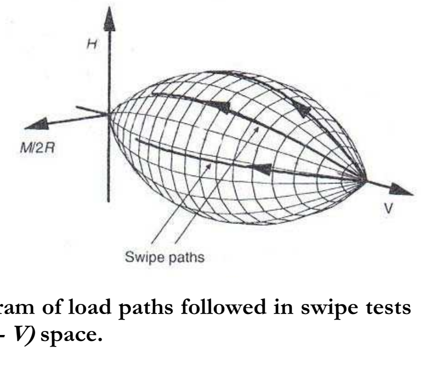

Figure 5.1. Schematic diagram of load paths followed in swipe tests [Gottardy et al., 1999] projected in a *(H - M/2R - V)* space.

Among all the tests realised by [Gottardy et al., 1999], 4 of them are studied and reproduced hereafter numerically with the new macro element (GG03, GG04, GG06 and GG07).

The test GG03 consists in applying a vertical displacement until a vertical force of V_0=1600N is reached. After that, the vertical displacement is kept constant while an increasing horizontal displacement is applied to the foundation (Figure 5.2).

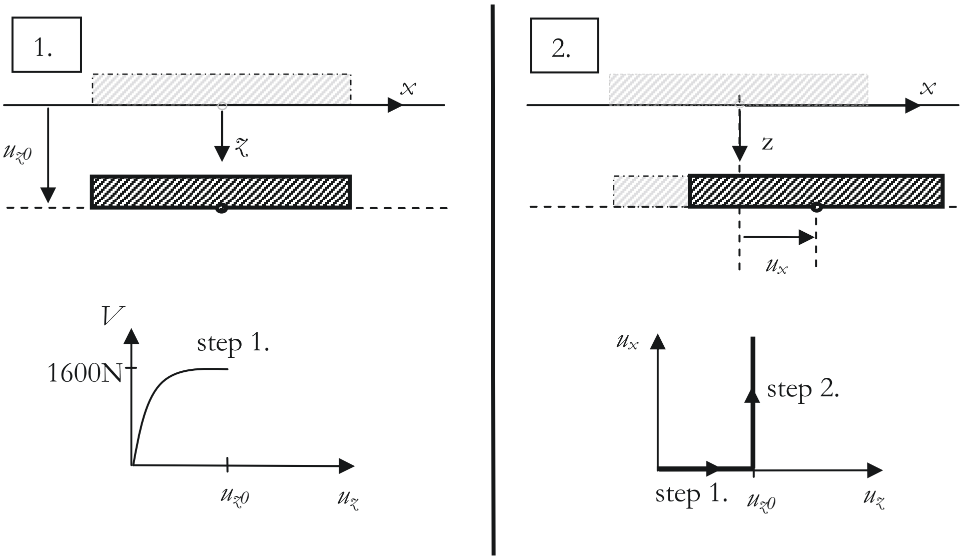

Figure 5.2. Swipe test GG03: Step 1. a constant vertical displacement is applied, Step 2. an increasing horizontal displacement is applied.

The test GG07 consists in applying a vertical displacement until V=1600N is reached (in order to develop isotropic hardening in the soil) and then the vertical displacement decreases to obtain an initial vertical force of V_0=200N. After that, the vertical displacement is - as before - kept constant while an increasing horizontal displacement is applied to the foundation (Figure 5.3).

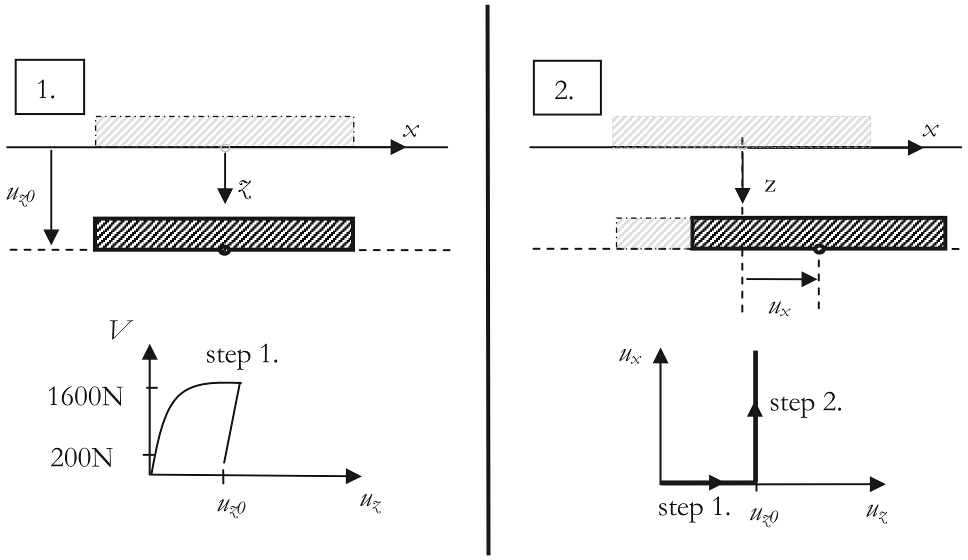

Figure 5.3. Swipe test GG07: Step 1. a constant vertical displacement is applied, Step 2. an increasing horizontal displacement is applied.

Figure 5.4 and Figure 5.5 show the load path in the planes (H_x -V) and (H_x-u_x) for the experimental test and the numerical test.

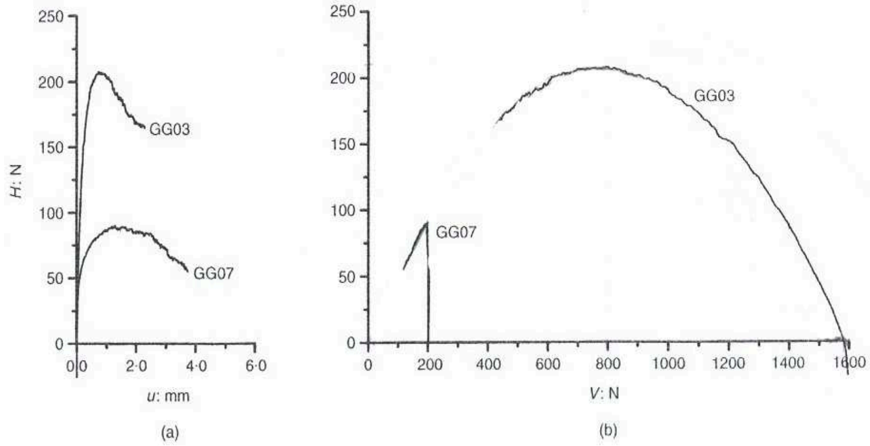

Figure 5.4. Experimental results for the swipe tests GG03 and GG07 in planes H_x-u_x and H_x-V

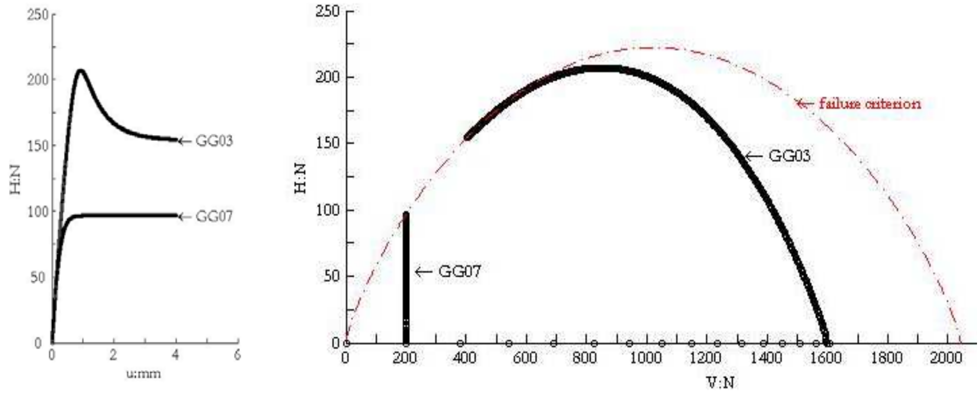

Figure 5.5. Numerical results for the swipe tests GG03 and GG07 in planes H_x-u_x and H_x-V.

Swipe test GG04 is realised in a similar way with the GG03 test. The only difference with GG03 is that after the initial vertical force of V_0=1600N is reached, an increasing rotation is applied to the foundation. Results are presented in Figure 5.6 and Figure 5.7.

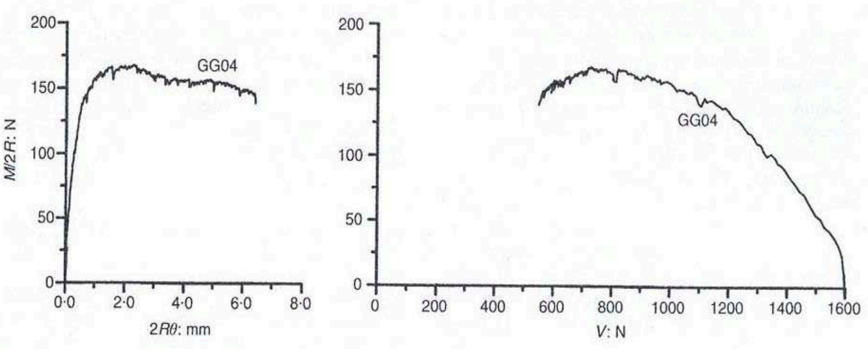

Figure 5.6. Experimental results for swipe test GG04 in planes $M_y/2R$-$2R\theta_y$ and $M_y/2R$ –V.

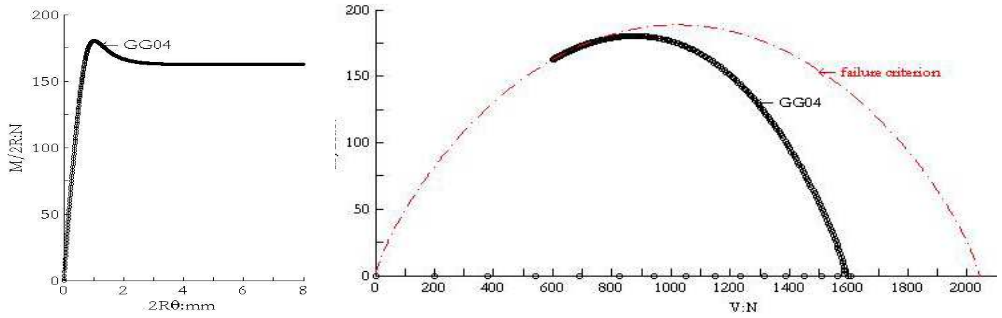

Figure 5.7. Numerical results for swipe test GG04 in planes $M_y/2R$-$2R\theta_y$ and $M_y/2R$ –V.

Finally, swipe tests GG06 and GG29 deal with a simultaneous horizontal displacement and rotation applied at the centre of the foundation with a constant ratio of: $\tan^{-1}(Dd\theta/du)=126°$ for GG06 and $\tan^{-1}(Dd\theta/du)=157°$ for GG29. This loading is applied again once the initial vertical load of V_0=1600N is reached imposing a constant vertical displacement. Figure 5.8 shows the experimental and numerical load paths in the plane ($h=H'_x/V_0$; $m=M'_y/(2RV_0)$):

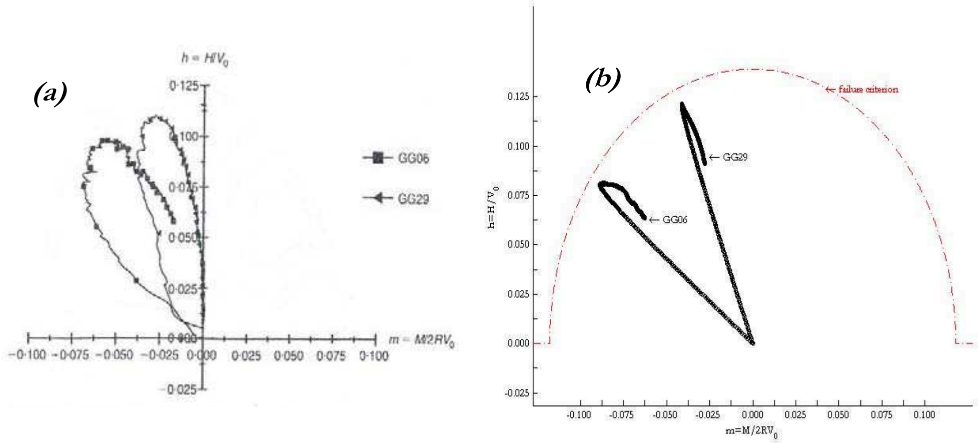

Figure 5.8. (a) Experimental results, (b) Numerical results for swipe tests GG06 and GG29 in plane *h-m*.

The parameters of the model are calibrated using the tests GG03 and GG04. Numerical results concerning the other tests are calculated without any further calibration. The previous diagrams show that the macro element is able to reproduce the trends of the behaviour of a circular footing under static loading when different combinations of displacements are imposed.

The horizontal displacement imposed during the test GG03 leads to a decrease of the vertical force. The explication is the following: the horizontal loading creates an isotropic hardening which develops plasticity in all directions, particularly in the V' direction. If the vertical load was an imposed vertical force, this increasing hardening in the direction V' would imply a plastic vertical displacement. Here however, the displacement is kept constant. This results to a decrease of the vertical force. V decreases from the initial value V_0=1600N to a constant value due to the fact that the sand was glued under the foundation implying a residual friction that can be computed through correct tuning of the flow rule parameters. The 3D macro element reproduces correctly this behaviour. It is interesting to notice that the load path follows particularly well the failure criterion of the experiment.

During the test GG07, the initial vertical loading of 1600N implies an increase of the size of the surface (isotropic hardening) before the horizontal displacement is applied. Then, while the horizontal displacement is increasing, the behaviour is quasi linear until the foundation reaches the stage of plasticity.

Test GG04 is also reproduced correctly by the macro element. Some differences concerning the peak of the curve on the (*M/2R, 2Rθ)* diagram are however noticeable.

Finally, for the tests GG06 and GG29, the loop is well simulated even if some differences exist. Theses differences come from the definition of the flow rule i.e. the relationship between the plastic displacement according to M'_y and H'_x. Calibrating the parameters of the model could lead to better numerical results.

In order to show the behaviour of the macro element under a 3D loading, the following numerical 3D swipe test is performed. Figure 5.9 shows the load path in the ($M_x/2R$-$M_y/2R$-V) space. At the beginning, a vertical displacement is imposed till a constant value and then the foundation is driven with an increasing rotation θ'_y until moment M'_y reaches a given value. At this stage this rotation is halted and kept constant, and a new increasing rotation θ'_x is applied to the foundation. Moments in the 2 directions are clearly developed and at the end the load path is very close to the failure surface.

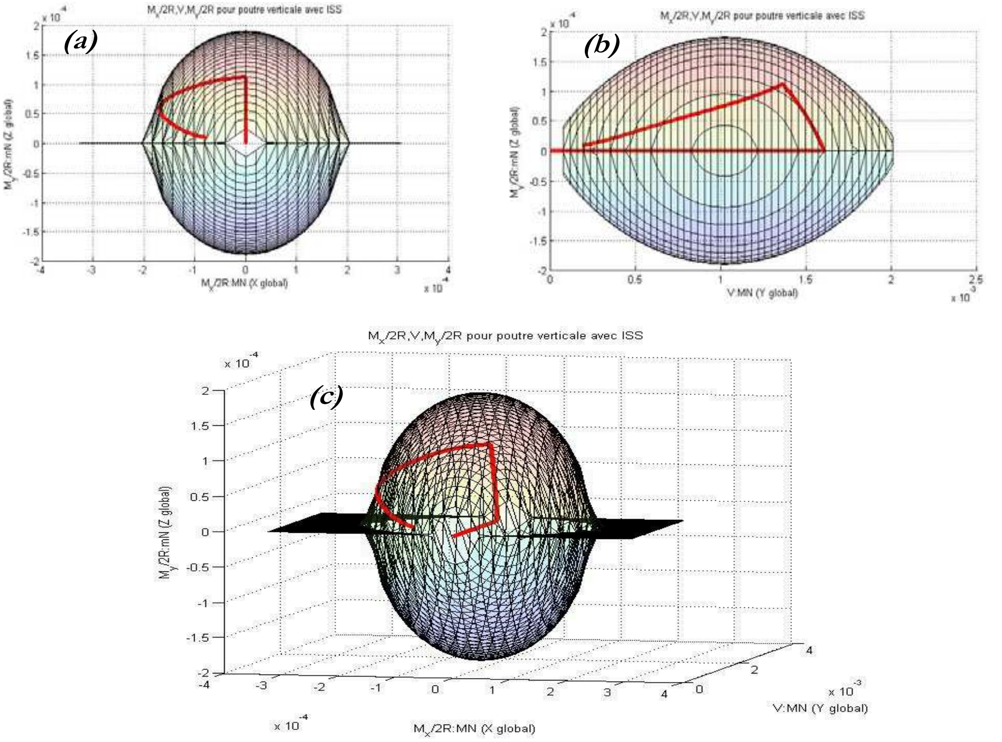

Figure 5.9. Numerical simulations of 3D swipe test: representation of the load path (curve in red) ***(a)*** **in planes** $M_y/2R$- $M_x/2R$, **(b)** $M_y/2R$-V, **(c) in space** $M_y/2R$- $M_x/2R$-V.

One has to remember that the philosophy of the 3D macro element and of the swipe tests is different. The swipe tests provide a loading surface for a given penetration which has the form of a "rugby" balloon. For a given penetration the loading surface of the 3D macro element is just a line. Once horizontal displacements or rotations are applied, the loading surface grows till embracing the failure criterion.

5.2 CYCLIC STATIC BEHAVIOUR

5.2.1 Virtual structure

To show that the model is able to reproduce the principal characteristics of a foundation submitted to a cyclic loading, a cyclic radial displacement is imposed at the top of a virtual slender structure embedded on a foundation. The slender structure is simulated using a 3D elastic beam and the foundation with the macro element (Figure 5.10).

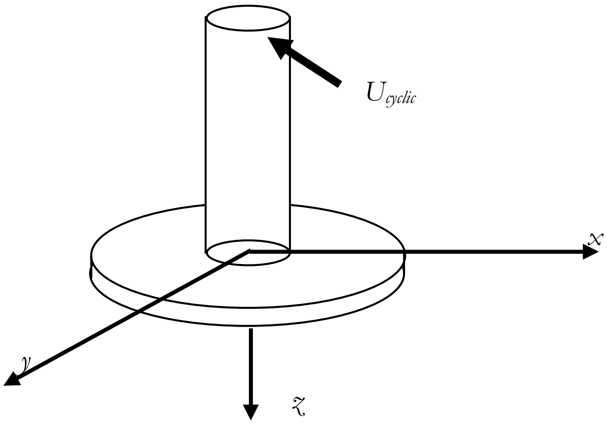

Figure 5.10. Representation of the virtual structure.

Figure 5.11 shows the evolution of the different forces compared to the associated displacements.

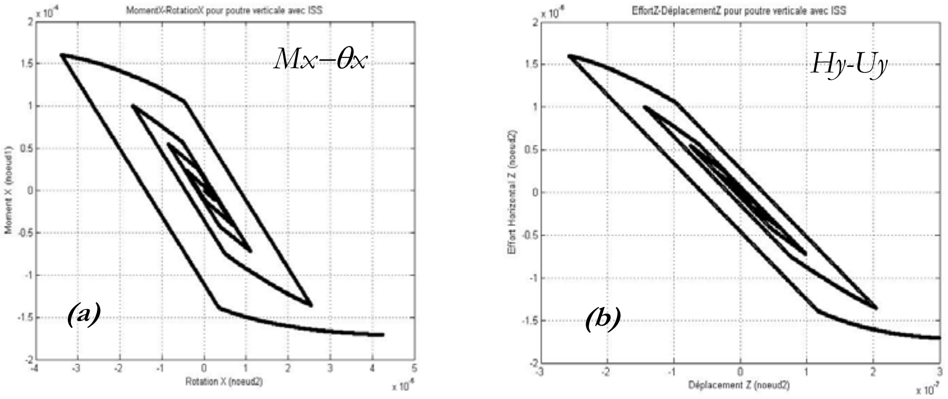

Figure 5.11. Cyclic behaviour considering rocking of the foundation.

The results are satisfactory as the macro element reproduces the two principal behaviours, mainly:

- The independence of the directions of loading (dM>0 and dM<0)
- The curve starts with the same slope when plasticity is recovered.

5.2.2 Cyclic behaviour of a foundation without rocking or uplift

By imposing $\dot{\rho} = 0$ (k=0) - in other words by adjusting the evolution of isotropic hardening compared to kinematic hardening -, it is possible to simulate the behaviour of a foundation lying on a low density soil or with low mechanical characteristics. In that case the behaviour of the foundation is without rocking or uplift.

Within the European program TRISEE, experimental tests are performed on a shallow 1m x 1m rectangular foundation lying on “Low density” sand [TRISEE, 1998]. Sine-shaped horizontal displacement cycles of increasing amplitude are applied at the top of a vertical beam embedded on the foundation (Figure 5.12).

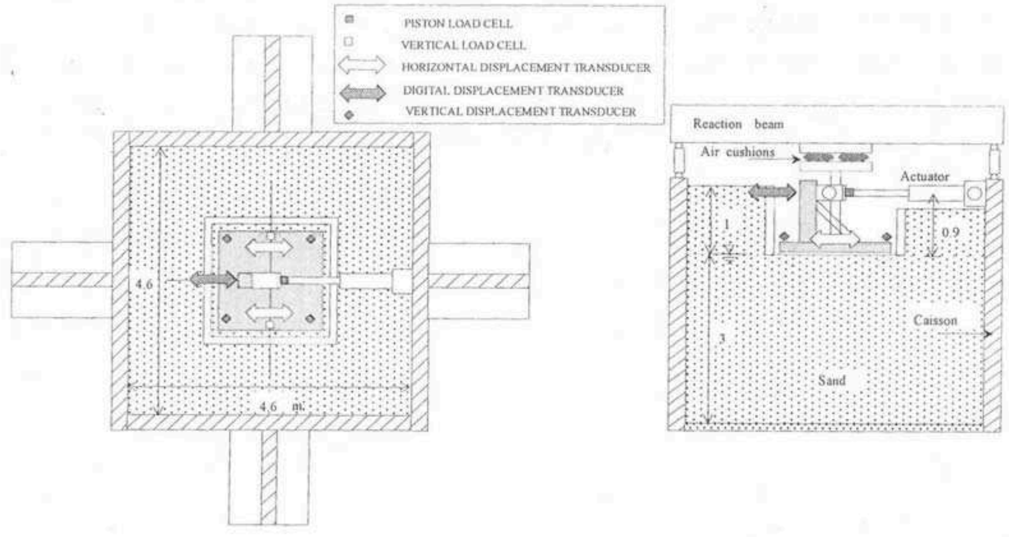

Figure 5.12. TRISEE: Scheme of the experimental mock-up (dimensions in m).

The macro element is developed to reproduce the 3D behaviour of a circular footing. The cyclic loading applied during the TRISSE test is a 2D one, thus the axisymmetric character of the macro element is not a limitation. The diameter of the numerical footing is calculated to have the same area with the experimental one. This leads to a diameter *D* equal to 1.128*m*.

Figure 5.13 shows the relationship between the horizontal force and the horizontal displacement reproduced numerically and during the experiment. Results are satisfactory in terms of the maximum horizontal forces. Nevertheless, the experimental loops move towards the negative direction of the horizontal displacements although the loading and the geometry of the mock-up are completely symmetric. A local failure could be the explanation of this behaviour. Numerical loops are completely symmetric because the macro element is not able to reproduce this local phenomenon.

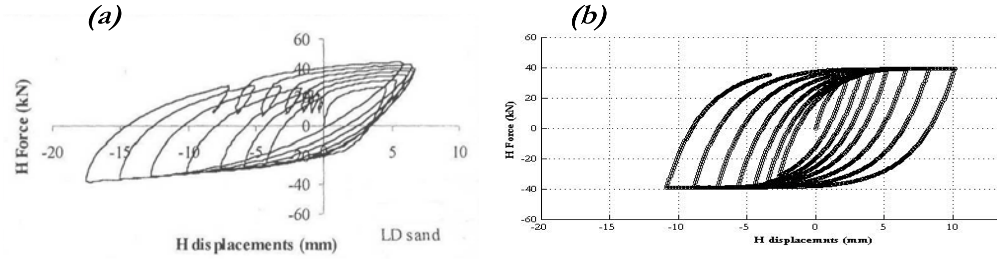

Figure 5.13. TRISEE: Comparison between (a) Experimental results and (b) Numerical results

Horizontal force vs. horizontal displacement.

Figure 5.14 shows the relationship between the moment and the rocking angle. Results are again very satisfactory. The main differences are that the moment reaches an asymptote (M_{lim}=40kNm) more quickly with the macro element that during the experiments. Once again the experimental curves are not symmetric but the phenomenon is less pronounced this time.

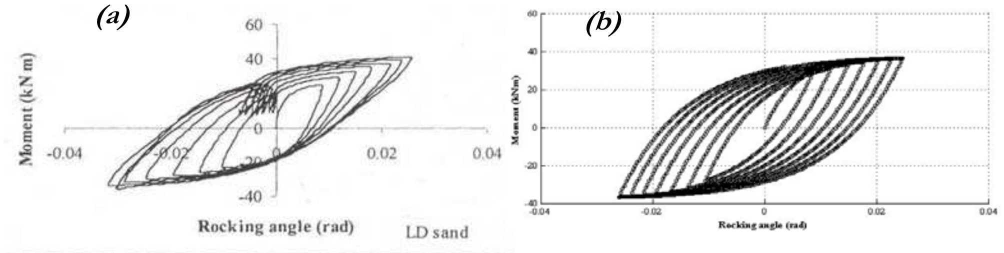

Figure 5.14. TRISEE: Comparison between (a) Experimental results and (b) Numerical results Moment vs. rocking angle.

Finally, Figure 5.15 presents the vertical settlement of the structure measured during the test and reproduced by the macro element. The different plateaus of the experimental curves are well simulated by the model, thanks to the good description of the plastic displacements by the flow rule. Nevertheless, experimental results show that the centre of the foundation rises from time to time slightly. Of course, the macro element cannot reproduce this behaviour because during the numerical simulation uplift and rocking are prohibited.

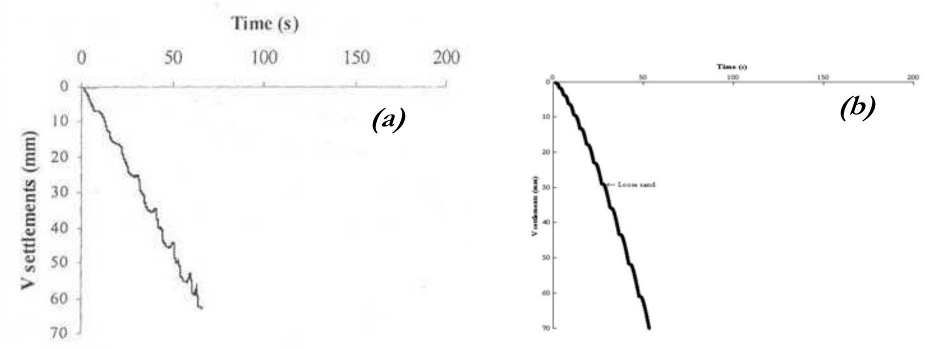

Figure 5.15. TRISEE: Comparison between (a) Experimental results and (b) Numerical results vertical settlement vs. time.

5.3 DYNAMIC BEHAVIOUR – CAMUS 4 TEST

In order to evaluate the efficiency of the macro element to predict the behaviour of a slender structure submitted to a dynamic loading, the simulation of the Camus 4 experiment [Combescure et al., 2000] is carried out.

5.3.1 Camus 4 test description

Camus 4 is an experiment in the line of a series of tests performed on seismic table realized in CEA Saclay. It is carried out within the framework of the European research projects ICONS-TMR[1], ECOEST II.

The mock-up represents a 5 storey building on a 1/3 scale. It is 5,1m high, and is made up of 2 reinforced concrete walls and 2 strip foundations of 0,8m x 2,1m (Figure 5.16). The mass of the structure equals 36.2t and the mass of the foundations is 2,3t (38.5t for the total). Camus 4 lies on a sand box of 4m x 4m (Figure 5.17). The mock-up is subjected to the Nice 0.33g earthquake motion applied in the direction of the walls.

Figure 5.16. Camus 4 - Mock-up.

Figure 5.17. Camus 4 - Sand box.

---

[1] Innovative design COncept for New and existing Structures - Training and Mobility of Researchers

5.3.2 Finite element mesh

A simple finite element mesh is used for the spatial discretization of the structure. The masses are concentrated at each floor and multifiber Timoshenko beam elements are used for the storeys (see Figure 5.18). Details about the masses and the elastic properties of the beam elements are presented in [Grange, 2004]. In order to simplify, the foundation is modelled using the macro element with a diameter *D*=2.1m.

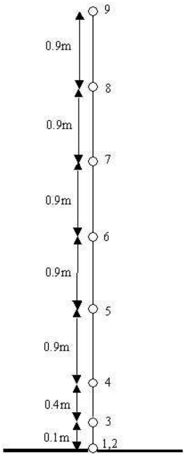

Figure 5.18. Camus 4 - Finite element mesh

Note: At the end of the experiment the structure underwent very little damage. That is the reason why the behaviour of the Timoshenko beams element is considered linear for the simulations presented hereafter.

5.3.3 Results

In all the graphs presented hereafter the red dotted lines correspond to the experimental results and the blue continuous ones to the numerical. The structure is submitted to the earthquake motion Nice 0,33g.

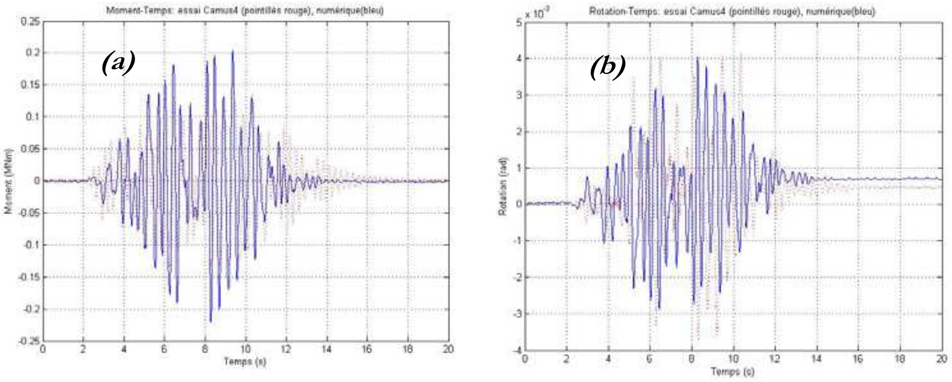

Figure 5.19. Camus 4 - Evolution of (a) moment and (b) rocking angle vs. time

Figure 5.19 shows the evolution of the moment at the base of the structure and the evolution of the rotation.

5.3.4 Comments

The main trends of the behaviour of the structure are quite well predicted:

- Experimental and numerical curves are relatively in phase.
- The values of the moment as well as the rotation at the base are well respected.

Nevertheless, some differences appear between the experimental and the numerical results. One has to remind that the macro element is initially developed to simulate a foundation lying on an infinite space. In the experimental test, the height of the sand box doesn't exceed 40cm. This experiment is beyond the domain of validity of the model. The elastic constant stiffness taking into account in the model could also explain the differences between experimental and numerical results. Indeed, actual stiffness is not a constant value but depends on the frequency of the waves in the soil.

It is interesting to notice that the macro element reproduces correctly the global behaviour of the Camus 4 specimen with a very small computational cost (only a couple of minutes are needed!) and with very simple finite element mesh (21 degrees of freedom).

6. BASE ISOLATORS AND DAMPERS

An important advantage of the macro element developed throughout this report is that by adjusting the parameters and by introducing different kinematic hardening laws it is relatively easy to reproduce the behaviour of different base isolators or dissipations devices. It is therefore possible to model the dynamic behaviour of structures where these kinds of isolators are introduced.

Classical base isolators dissipate energy only through shear deformation. This is the reason why only horizontal forces and displacements need to be computed and so the 3D macro element can be greatly simplified. Indeed, moments and vertical components are transmitted to the structure relatively unchanged. Moreover, the 2 horizontal directions x and y for the displacements and forces can now be considered totally uncoupled. The non-interpenetration criterion (or tangency rule) is also highly simplified. Stiffness parameters and parameters of the failure criterion can be easily fitted using experimental results (horizontal forces - horizontal displacements) for different kind of isolators.

3 kinds of isolators are presented hereafter. The first one is an elastomeric bearing base isolator which can be placed at the base of a structure. The 2 others are dissipation devices placed for example in a diagonal bracing mechanism.

6.1 BASE ISOLATOR DEVICE

The base isolator studied hereafter is composed of laminated rubber bearings. Details of the specimen are shown in Figure 6.1 and Figure 6.2, [Chung et al., 1999].

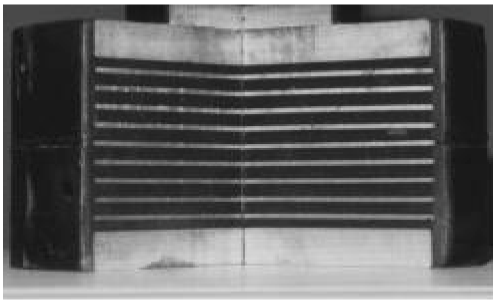

Figure 6.1. Cross-section of base isolator.

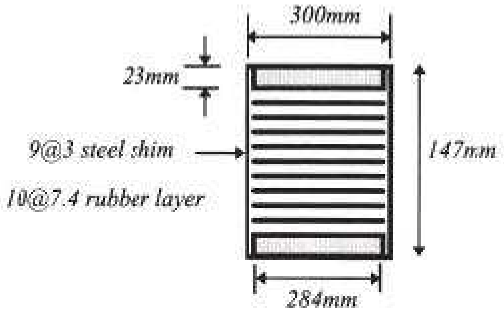

Figure 6.2.Details of the base isolator [Chung et al., 1999]

A particularity of this type of isolator is that the experimental restoring force does not seem to attend a plateau even for high displacements. In other words, kinematic hardening always increases even for high displacements (Figure 6.3, [Chung et al., 1999]). That's why the kinematic hardening evolution used in the macro element is modified by the addition of a term in order to obtain an oblique asymptote [Lemaitre et al., 1988] (instead of the horizontal asymptote for the initial 3D macro element). A new parameter is thus introduced to parameterize the slope of this asymptote. Numerical results compared to experimental simulations are presented in Figure 6.3.

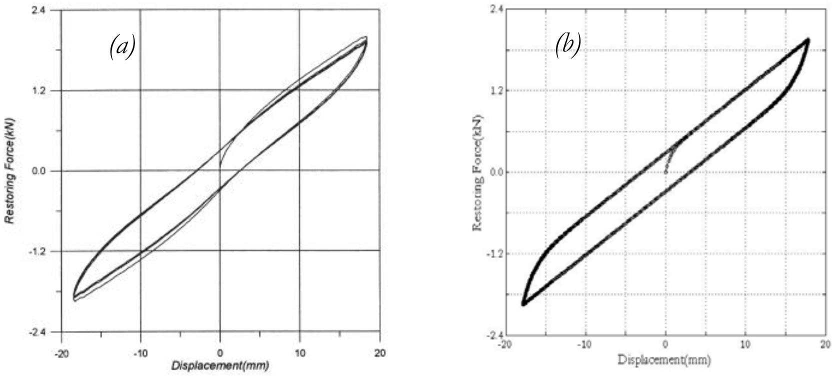

Figure 6.3. Base isolator - Relationship between horizontal force and displacement: (a) Experimental results, and (b) numerical results.

Numerical results are very close to the experimental results. In particular, the size of the loop is well described, permitting to have a good approximation of the hysteretic damping behaviour of the isolator.

6.2 DISSIPATION DEVICES

6.2.1 Metallic dampers

Placed into the skeleton of a structure, metallic dampers dissipate energy trough hysteretic behaviour of metals when they behave plastically. Figure 6.4 shows the Triangular Added Damping And Stiffness (TADAS) device which is made of triangular steel plates [Chopra, 1995].

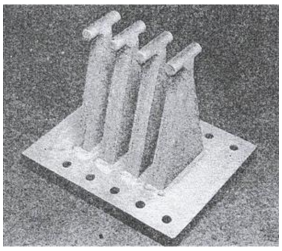

Figure 6.4. TADAS device [Chopra, 1995]

The loops described by this type of dampers are stable (Figure 6.5), and present a horizontal asymptote. This behaviour is well predicted by the 3D macro element when uplift and rocking are cancelled. As was the case for the base isolator, parameters of the model are easy to fit (parameters of the loading surface permit to adjust the plateau of the curve and the elastic stiffness permit to adjust the slope at the origin).

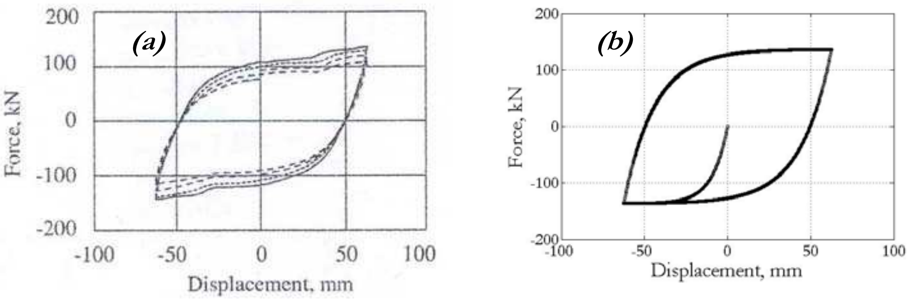

Figure 6.5. TADAS device - Relationship between force and displacement: (a) Experimental results [Chopra, 1995], and (b) numerical results.

6.2.2 Friction dampers

Adopting a similar philosophy with the metallic dampers, friction dampers permit to dissipate the energy by friction between several plates. A schematic diagram of this kind of damper is given in Figure 6.6 [Chopra, 1995]. Again, behaviour is well predicted using the macro element when uplift and rocking are cancelled. Here the elastic stiffness is chosen with a very high value to obtain the rectangular loops (see Figure 6.7).

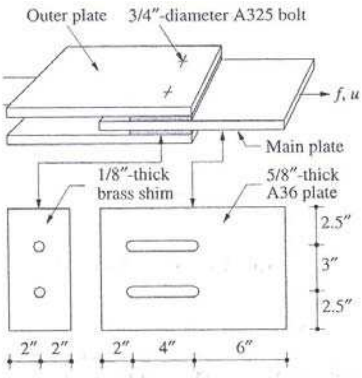

Figure 6.6. Friction damper device [Chopra, 1995].

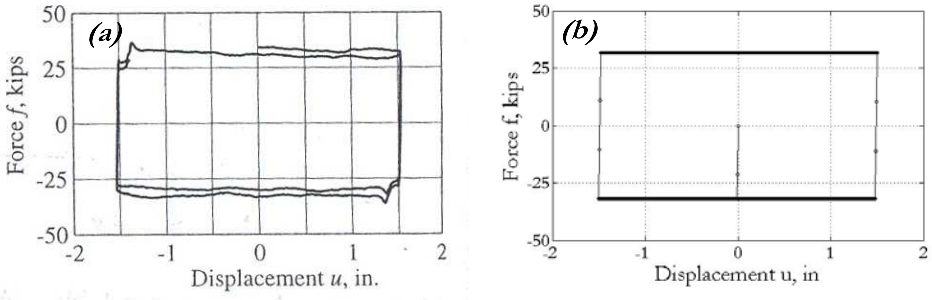

Figure 6.7. Friction dampers - Relationship between force and displacement: (a) Experimental results [Chopra, 1995], and (b) numerical results.

As a conclusion the 3D macro element can be adapted to simulate the behaviour of different base isolators and dissipative devices. Adapting the model is a very simple procedure consisting for example in modifying the kinematic hardening in order to obtain an oblique asymptote. Uncoupling of the different directions is also possible, thus computation is simplified.

7. CONCLUSION AND WAY FORWARD

The 3D macro element developed within this work gives satisfactory results for simulating the non linear behaviour of a circular rigid foundation lying on an infinite space submitted to a monotonic static but also cyclic or dynamic loading. Using global variables it presents the advantage of inducing low computation costs. This first version of the 3D macro element is implemented in the Matlab toolbox FedeasLab.

Nevertheless, different improvements could be done, in particularly concerning the fitting of the parameters (stiffness, shape of the loading surface) and the different rules (flow rule, tangency rule). The difficulty to develop a macro element in 3D lies in the fact that it has to be capable of simulating a non radial loading. Indeed, in 3D, forces and moments in the 2 horizontal directions x and y are coupled with a non linear relation (whereas the 2D original version of the macro element was developed by considering linearity between the horizontal force H'_x and the moment M'_y). The tangency rule, function that manages the evolution of the load surface is thus complicate and need to be improved.

The new Deliverable D8-2 of the LESSLOSS program (deliverable under preparation) has the objective of presenting extensive validations of the 3D macro element with further experimental and numerical results.

REFERENCES

CAMUS International Benchmark. [1997]. "Mock-up and loading characteristics, specifications for the participants report". Report I. CEA and GEO.

Cassidy, M.J., Byrne, B.W., and Houlsby, G.T. [2002]. "Modelling the behaviour of circular footings under combined loading on loose carbonate sand". *Géotechnique,* Vol 52, No. 10, pp. 705-712.

Chopra, A.K. [1995]. *Dynamics of Structures: Theory and Applications to Earthquake Engineering*, Prentice Hall.

Chung, W.J., Yun, C.B., Kim, N.S., Seo, J.W., [1999] "Shaking table and pseudodynamic tests for the evaluation of the seismic performance of based isolated structure", *Engineering Structures*, Vol. 21, pp 365-379.

Combescure, D. and. Chaudat, Th. [2000] "ICONS european program seismic tests on r/c walls with uplift; camus iv specimen", Individual Study, ICONS project Rapport, SEMT/EMSI/RT/00-27/4, CEA, Direction des Réacteurs Nucléaires, Département de Mécanique et de Technologie, 2000, Paris, France.

Crémer, C. [2001] "Modélisation du comportement non linéaire des fondations superficielles sous séismes", *PhD Thesis*, LMT Cachan - ENS Cachan, France.

Crémer, C., Pecker, A., Davenne, L. [2001] "Cyclic macro-element for soil-structure interaction: material and geometrical non-linearities", *International Journal for Numerical and Analytical Methods in Geomechanics*, Vol. 25, No. 13, pp. 1257-1284.

Crémer, C., Pecker, A., Davenne, L. [2002] "Modelling of nonlinear dynamic behaviour of a shallow strip foundation with macro-element", *Journal of Earthquake Engineering*, Vol. 6, No. 2, pp. 175-211.

Filippou, F.C. and Constandines, M. [2004] *FedeasLab Getting Started Guide And Simulations Examples*. Dpt of civil and env. Engng. UC Berkeley

Gazetas, G. [1991] "Foundations vibrations". In *Foundation Engineering Handbook*, Chapter 15. Fang H-Y (ed.), van Nostrand Reinhold: New York.

Gottardy, G., Houlsby, G.T. and Butterfield, R. [1999] "Plastic response of circular footings under general planar loading," *Géotechnique*, Vol. 49, No. 4, pp. 453-469.

Grange, S., [2004] "Modéliastion du comportement non linéaire de l'interaction sol structure sous séismes", *Mémoire de stage du Master Recherche 2 MCGM*, INPG, UJF, ENS Cachan.

Lemaitre, J. and Chaboche, J.L. [1988]. "Mécanique des matériaux solides", Dunod, Bordas, Paris, France.

Nova, R. and Montrasio, L. [1991]. "Settlements of shallow foundations on sand," *Géotechnique*, Vol. 41, No. 2, pp 243-256.

Pecker, A. [1984] *Dynamique des sols*. Presse, ENPC, Paris, France.

Pecker, A. [1997] *Analytical formulae for the seismic bearing capacity of shallow strip foundations*, Balkema, Rotterdam, editor, Netherlands.

Simo, J.C. and Hughes, T.J.R. [1998] *Computational Inelasticity*, Mechanics and materials, Springer Interdisciplinary applied mathematics vol.7.

TRISEE, [1998] 3D Site Effects and Soil-Foundation Interaction in Earthquake and vibration Risk Evaluation, Part 4 "Large-scale geotechnical experiments on soil-foundation interaction," European Commission, Directorate General XII for science, Research and Development.